Neutron-Capture Reaction Rate Uncertainties for the I-Process in He-Shell Flash White Dwarfs from Monte-Carlo Simulations

Pavel Denisenkov[1,2,9], Christian Ritter[1,2,9], Marco Pignatari[3,4,9], Samuel Jones[8,9], Stylianos Nikas[2,6], Georgios Perdikakis[2,5,6], Hendrik Schatz[2,5,7,9], Artemis Spyrou[2,5,7] and Falk Herwig[1,2,9]

1 Department of Physics and Astronomy, University of Victoria, Victoria, BC, V8W 2Y2, CANADA. 2 JINA-CEE, Michigan State University, East Lansing, MI, 48824, USA. 3 Department of Physics and Mathematics, University of Hull, HU6 7RX, UK. 4 Konkoly Observatory, Hungarian Academy of Sciences, 1121 Budapest, Hungary. 5 NSCL Michigan State University, East Lansing, MI, 48824, USA. 6 Department of Physics, Central Michigan University, Mt. Pleasant, MI, 48859, USA. 7 Department of Physics and Astronomy, Michigan State University, East Lansing, MI, 48824, USA. 8 Heidelberg Institute for Theoretical Studies, 69118 Heidelberg, Germany. 9 NuGrid Collaboration, **URL:** *http://www.nugridstars.org.*

§1. Monte-Carlo (MC) simulations

Problem: the observed and predicted abundances of Rb, Sr , Y, and Zr in Sakurai's object (V4334 Sagittarii) do not match (Figure 1).
Solution: we investigate stellar physics and nuclear reaction rate uncertainties to identify those responsible for this mismatch.
Here, we analyze the impact of uncertainties in the (n,γ) cross sections of unstable isotopes near N=50 (Figure 2) on the **i-process** nucleosynthesis, that includes the production of Rb, Sr, Y and Zr, using the results of our Monte-Carlo (MC) simulations.
In the **i process,** the neutron density can reach a value of ~10^{15} cm^{-3}, intermediate between those typical for the s- and r-processes. Cowan and Rose (1977, ApJ, 212, 149) have shown that the i process is activated when He-shell flash convection ingests H from a surrounding H-rich envelope, neutrons being released via ^{12}C(p,γ)^{13}N(e$^+$ν)^{13}C(α,n)^{16}O. This can happen during a very late thermal pulse (VLTP) of a He shell in a post-AGB star, such as Sakurai's object, or during multiple He-shell flashes, intermittent with stationary H burning, in rapidly accreting white dwarfs (RAWDs) in close binary systems.
Method: we run the NuGrid multi-zone post-processing nucleosynthesis parallel code **mppnp** 10000 times. Our MC simulations have the same model setup for the i-process nucleosynthesis in the convective He shell of Sakurai's object, but they use different sets of the multiplication factors for the (n,γ) cross sections of the 52 unstable isotopes shown in Figure 2. For each of these isotopes, a random number is first selected from a uniform distribution between 1 and the maximum variation factor corresponding to this isotope that was constrained by uncertainties in the Hauser-Feshbach calculations and that is color-coded in Figure 2, then this number or its inverse value is assigned to the multiplication factor with an equal probability. To reduce the total computational time, we use a small network of 441 isotopes up to Ag, which does not affect the final abundances of the lighter elements (Figure 3). **Results:** as an example, the green histogram in Figure 4 shows the distribution of the surface abundance of Zr in Sakurai's object from our MC simulations. It was fitted with a normal distribution to estimate its mean and dispersion. The same Zr histogram is presented in Figure 5, using varying circle size and color, while its corresponding mean and dispersion being plotted as black square with error bars, along with the MC results for the other elements of the s-process peak. From Figure 5, we conclude that the uncertainties in the final surface abundances due to the uncertainties in the relevant (n,γ) cross sections are less than or comparable to the observational errors. Figure 6 shows the MC simulation that best fits the observed abundances.

§2. Analysis of the first (D1) and second (D2) partial derivatives

Method: here, we compute and analyze the changes of the surface abundances of Rb, Sr, Y, and Zr in the model of Sakurai's object ensuing when the maximum up and down variations of the multiplication factors from Figure 2 are applied to one (n,γ) reaction rate per simulation (case D1, 104 simulations) and to a pair of (n,γ) reaction rates per simulation (case D2, 5304 simulations). This method allows us to identify the unstable isotopes near N=50 and their pairs whose (n,γ) cross-section variations lead to the largest changes in the final surface abundances.
Results: Figures 7 and 8 along with Figure 9 help to visualize our results. Their numerical analysis identifies the following isotopes as the ones leading to the largest changes in the final abundances of the first s-process peak elements when their (n,γ) cross sections are multiplied (up) and divided (down) by their corresponding maximum variation factors from Figure 2:

For the abundances of individual elements (the mass fraction changes ΔX)

1. D1: ^{88}Kr (ΔX(Rb)=0.23dex); D2: the pair of ^{85}Br and ^{88}Kr (ΔX(Rb)=0.49dex).
2. D1: ^{89}Kr (ΔX(Sr)=0.31dex); D2: the pair of ^{87}Kr and ^{88}Kr (ΔX(Sr)=0.53dex).
3. D1: ^{90}Kr (ΔX(Y)=0.28dex); D2: the pair of ^{88}Kr and ^{89}Rb (ΔX(Y)=0.53dex).
4. D1: ^{89}Kr (ΔX(Zr)=0.24dex); D2: the pair of ^{88}Kr and ^{89}Rb (ΔX(Zr)=0.34dex).

For the elemental abundance ratios

1. D1: ^{88}Kr (Δ[Rb/Sr]=0.51); D2: the pair of ^{87}Kr and ^{88}Kr (Δ[Rb/Sr]=0.76).
2. D1: ^{89}Kr (Δ[Y/Sr]=0.46); D2: the pair of ^{88}Kr and ^{89}Rb (Δ[Y/Sr]=0.72).
3. D1: ^{89}Rb (Δ[Zr/Y]=0.33); D2: the pair of ^{89}Kr and ^{89}Rb (Δ[Zr/Y]=0.58).

Figures 10 and 11 show the best fits of the observed abundances from the D2 and D1 simulations.
Conclusion: the (n,γ) cross sections of ^{85}Br, ^{87}Kr, ^{88}Kr, ^{89}Kr, ^{90}Kr, and ^{89}Rb are worth measuring experimentally in the first turn in relation to the discussed problem.

§3. The D1 and D2 results of one-zone simulations

Method: here, we check if the one-zone model (with constant temperature and density) of the i process in Sakurai's object provides the same results as the multi-zone model. Figure 12 shows our choice of the one-zone benchmark model that has the abundances of Rb, Sr, Y, and Zr as close as possible to those obtained with the multi-zone benchmark model.
Results: (compare to §2)

For the abundances of individual elements (the mass fraction changes ΔX)

1. D1: ^{85}Br (ΔX(Rb)=0.18dex); D2: ^{85}Br and ^{87}Br (ΔX(Rb)=0.62dex).
2. D1: ^{85}Br (ΔX(Sr)=0.36dex); D2: ^{85}Br and ^{88}Kr (ΔX(Sr)=0.63dex).
3. D1: ^{89}Kr (ΔX(Y)=0.65dex); D2: ^{85}Br and ^{89}Kr (ΔX(Y)=1.15dex).
4. D1: ^{85}Br (ΔX(Zr)=0.44dex); D2: ^{85}Br and ^{88}Kr (ΔX(Zr)=0.78dex).

For the elemental abundance ratios

1. D1: ^{85}Br (Δ[Rb/Sr]=0.52); D2: ^{85}Br and ^{87}Kr (Δ[Rb/Sr]=0.85).
2. D1: ^{89}Kr (Δ[Y/Sr]=0.70); D2: ^{88}Kr and ^{89}Kr (Δ[Y/Sr]=1.02).
3. D1: ^{89}Kr (Δ[Zr/Y]=0.78); D2: ^{89}Br and ^{89}Kr (Δ[Zr/Y]=0.90).

Figures 13 and 14 show the best fits of the observed abundances from the D2 and D1 one-zone simulations.
Conclusion: the (n,γ) cross sections of ^{85}Br, ^{87}Br, ^{87}Kr, ^{88}Kr, and ^{89}Kr are worth measuring experimentally in the first turn in relation to the discussed problem. This list overlaps with the one recommended in §2, but it also includes ^{87}Br and misses ^{90}Kr and ^{89}Rb, therefore, if computational resources allow, the preference should be given to multi-zone simulations.

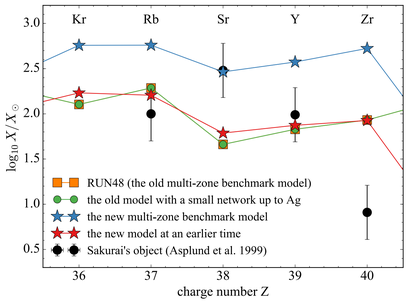

Figure 1: The surface mass fractions of the first s-process peak elements predicted by different multi-zone models of the i process in Sakurai's object compared to those observed by Asplund et al. (1999, A&A, 343, 507). The RUN48 model was used by Herwig et al. (2011, ApJ, 727, 89). The red stars are the results obtained with the new benchmark model that is used in the present work, in which the final abundances in the convective He-shell are averaged over its mass and allowed to decay for 2 years of the lifetime of Sakurai's object.

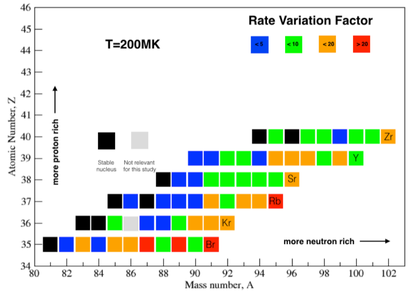

Figure 2: The maximum variation factors for the (n,γ) cross sections of unstable isotopes near N=50 constrained by Hauser-Feshbach calculations with different physics input data and model assumptions. They are used to determine the limits of changes (up and down) of the randomly selected multiplication factors for the corresponding (n,γ) reaction rates in our MC uncertainty investigation.

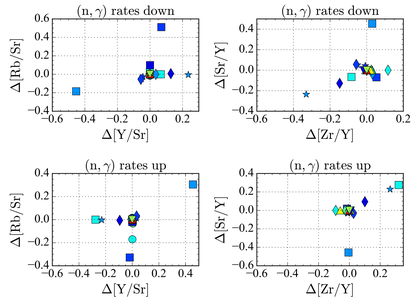

Figure 7: The scatter of the logarithmic surface abundance ratios in the multi-zone model of the i process in Sakurai's object produced by the maximum variations (up and down) of the (n,γ) cross section of just one isotope from Figure 2 per simulation (the D1 case). This plot uses the color- and shape-coding scheme from Figure 9.

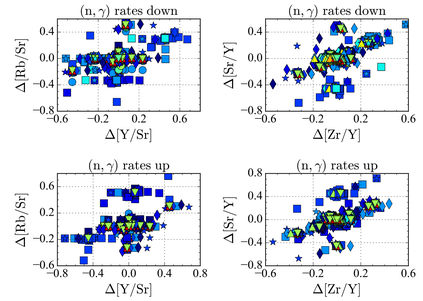

Figure 8: Same as in Figure 7, but for the D2 case in which the (n,γ) cross sections of a pair of isotopes have been varied simultaneously, using their maximum variation factors (up and down) from Figure 2, per simulation. In this scatter plot the second isotope of the pair overlaps the first one.

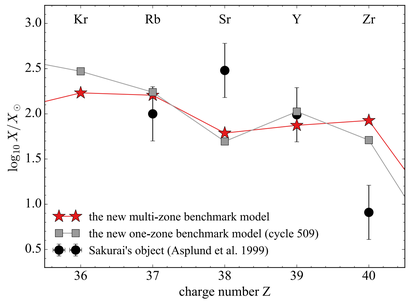

Figure 12: The one-zone benchmark model of the i process in Sakurai's object has the abundances of Rb, Sr, Y, and Zr as close as possible to those obtained in the multi-zone model. Our one-zone model also allows the final abundances to decay for 2 years.

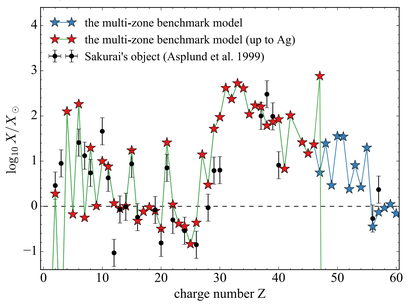

Figure:3 The results of a test demonstrating that our using of a small network of 441 isotopes up to Ag in the new benchmark model of Sakurai's object does not affect the abundances of the elements lighter than Ag, while it allows to significantly reduce the computational time.

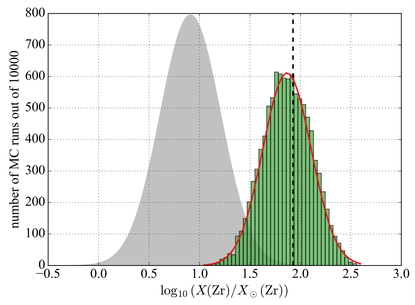

Figure:4 The distribution of the predicted surface mass fractions of Zr from our MC simulations (the green histogram). The vertical dashed line is the benchmark model prediction. By fitting a normal distribution (the red curve), we estimate the mean and dispersion of the results. For comparison, the grey-shaded area shows the observed Zr abundance represented by a normal distribution with the mean and dispersion from Asplund et al. (1999, A&A, 343, 507).

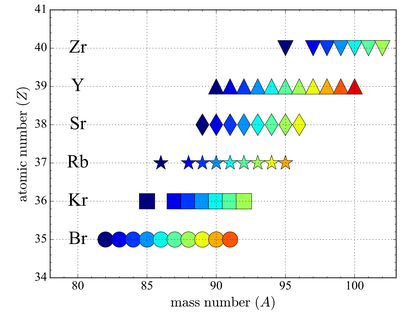

Figure 9: The color- and shape-coding scheme used to identify the isotopes whose (n,γ) cross-section maximum variations (up and down) have produced the scatters of the final abundance ratios shown in Figures 7 and 8.

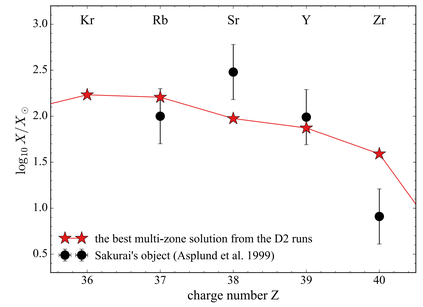

Figure 10: The best-fitted solution from the D2 multi-zone simulations.

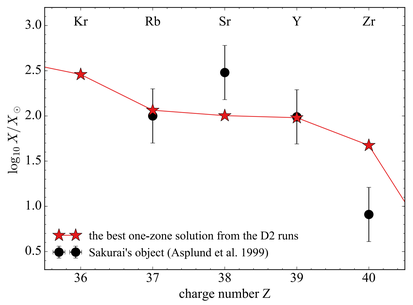

Figure 13: The best-fitted solution from the D2 one-zone simulations.

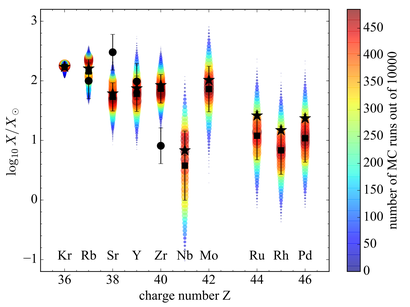

Figure 5: The circle color- and size-coded distributions of the final surface mass fractions of the first s-process peak elements from our MC simulations. The star symbols are the benchmark model predictions. The squares with error bars show the mean values and dispersions of the presented distributions estimated as explained in Figure 4. This plot demonstrates the effects of the (n,γ) reaction rate uncertainties on the predicted abundances. They turn out **to be less than or comparable to the observational errors**.

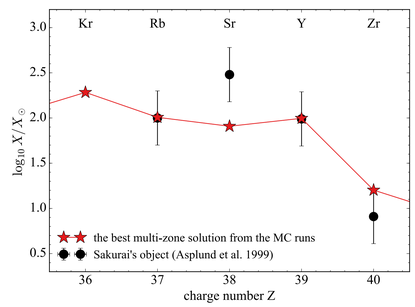

Figure 6: The results of the MC simulation that best fits the observed abundances.

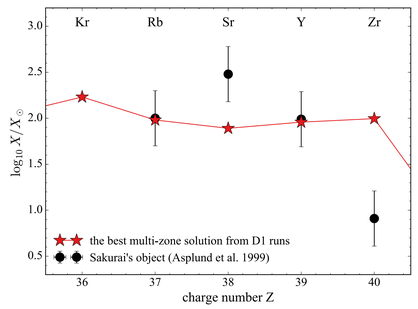

Figure 11: The best-fitted solution from the D1 multi-zone simulations.

Acknowledgments. M. P. acknowledges the support from the "Lendület-2014" Programme of the Hungarian Academy of Sciences and from SNF (Switzerland). F. H. receives NSERC funding through a Discovery grant. S. J. is a fellow of the Alexander von Humboldt Foundation and acknowledges support from the Klaus Tschira Stiftung. The computations for this work were made on the supercomputer Mammouth Parallèle 2 from the University of Sherbrooke, managed by Calcul Québec and Compute Canada. The operation of this supercomputer is funded by the Canada Foundation for Innovation (CFI), the ministère de l'Économie, de la science et de l'innovation du Québec (MESI) and the Fonds de recherche du Québec – Nature et technologies (FRQ-NT).

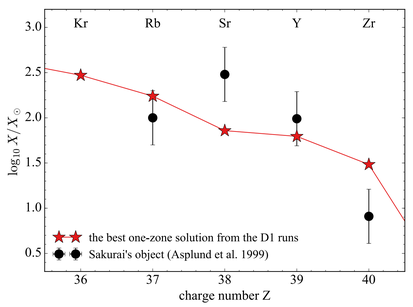

Figure 14: The best-fitted solution from the D1 one-zone simulations.

This material is based upon work supported by the National Science Foundation under Grant No. PHY-1430152 (JINA Center for the Evolution of the Elements).